



The influence of microstructural orientation on fracture toughness in (V, Al)N and (V, Al)(O, N) coatings as measured by microcantilever bending

Markus R. Schoof^{1,a)} , S. Karimi Aghda², C. F. Kusche¹, M. Hans², J. M. Schneider², S. Korte-Kerzel¹, J. S. K.-L. Gibson¹

¹Institute of Physical Metallurgy and Materials Physics, RWTH Aachen University, Kopernikusstraße 14, 52074 Aachen, Germany

²Materials Chemistry, RWTH Aachen University, Kopernikusstraße 10, 52074 Aachen, Germany

^{a)}Address all correspondence to this author. e-mail: schoof@imm.rwth-aachen.de

Received: 9 November 2022; accepted: 5 July 2023; published online: 7 August 2023

Since protective transition metal (oxy)nitride coatings are widely used, understanding of the mechanisms linking microstructure to their fracture behaviour is required to optimise wear resistance, while maintaining fracture toughness. To assess this interconnection, beam bending was performed using microcantilevers oriented parallel and at 90° to the growth direction. Furthermore, the tests were applied to favour normal bending and shear fracture. Coatings were synthesised by both direct current magnetron sputtering (DCMS) as well as high power pulsed magnetron sputtering (HPPMS). Here, we show that the fracture toughness depends on the alignment of the grains and loading directions. Furthermore, an improved fracture toughness was found in coatings produced by HPPMS, when microstructural defects, such as underdense regions in DCMS deposited coatings can be excluded. We propose indices based on fracture and mechanical properties to rank those coatings. Here, the HPPMS deposited oxynitride showed the best combination of mechanical properties and fracture toughness.

Introduction

Investigations on the applicability of thin protective coatings deposited via physical vapour deposition (PVD) for industrial applications [1–5], such as cubic transition metal aluminium nitrides c-(TM, Al)N (space group $Fm\bar{3}m$, NaCl prototype structure), are of interest due to the coatings' excellent properties like high hardness and elasticity [6–8] or good thermal stability [9, 10] and electrical conductivity [11–13]. In addition, the quaternary compounds of (TM, Al)(O, N) have recently drawn attention [14–16]. Incorporation of oxygen resulted in the reduction of flank wear of (Ti, Al)N coatings from 0.07 to 0.04 mm due to improved oxidation resistance of (Ti, Al)(O, N) [17]. In addition, Holzapfel et al. have recently shown that oxygen incorporation in the metastable c-(Ti, Al)N would result in thermal stability enhancement of quaternary (Ti, Al)(O, N) by up to 300 °C. The metastable nature of c-(TM, Al)N and c-(TM, Al)(O, N) requires non-equilibrium processing routes. Two widely applied processes to synthesise these coatings are direct current magnetron sputtering, DCMS [18] and

high power pulsed magnetron sputtering, HPPMS [19]. While in DCMS the plasma is dominated by gas ions [20], in HPPMS a significant fraction of metal ions are present [21] and therefore a denser coating is achieved, which can result in enhanced mechanical properties [22]. Within the non-equilibrium processing conditions discussed above, the kinetic limitation of low adatom mobilities mostly results in competitive growth of V-shaped columnar structures [23]. Under mechanical loading, the weak column boundaries have been shown to act as susceptible spots through which the crack initiation and propagation takes place. Coatings deposited by DCMS normally show a higher deposition rate, but a lower density and rougher surface [24]. By using stronger magnetrons [25] and a higher substrate bias potential, the density can be increased and surface roughness decreased as shown for the coatings deposited by HPPMS process [26]. Nevertheless, the strength of the magnetron and the choice between DCMS and HPPMS does not necessarily cause changes in grain size as Hajihoseini and Gudmundsson [25] revealed. There are several studies on binary TMNs, such

as TiN [27, 28], VN [6], or CrN [29], but the majority of recent research has focussed on their ternary systems, where aluminium was added to improve mechanical properties [28, 30, 31] and oxidation resistance [32–35].

Used in applications such as cutting tools or in polymer forming, (TM, Al)(O, N) coatings are exposed to diverse lateral and axial forces that may deform and damage the coating. Thus, studying the mechanical behaviour of these coatings becomes essential and various micromechanical test methods such as nanoindentation [36–39] and micropillar compression [40–42] have been used so far. A commonly used property to describe the fracture behaviour is the fracture toughness. It was shown that the fracture toughness can be estimated by means of nanoindentation [43]. However, as this method is affected by residual stresses [44], micro-beam bending is mostly used [45]. In numerous studies [46–49] the effects of size and geometry of those beams have been highlighted and the relation between stiffness and crack length was established [50, 51]. In addition, Matoy et al. calculated the critical crack energy for crack initiation in hard coatings [52, 53].

Beam bending tests [32, 54–56] have been carried out for transition metal aluminium nitride coatings with different chemical compositions. The effect of the chemical composition remains unclear and is easily convoluted where the substrate is changed concurrently. For example, in a study by Gibson et al. (V, Al)N showed a higher fracture toughness than (Ti, Al)N on a silicon substrate [54], while on a copper substrate the trend is reversed [55]. The incorporation of oxygen revealed a decrease in elastic stiffness due to the formation of relatively weak metal–oxygen bonds and metal vacancies [57] and thus, results in a lower fracture toughness [54]. Another strategy to improve fracture toughness without changing the chemical composition is to tailor the coatings' microstructure, in particular in terms of grain and column size or aspect ratio and by the addition of further internal interfaces. The latter is realised by the deposition of nanolaminates [58–60], which have been found to increase fracture toughness by crack deflection [61].

Here, cantilever bending is used to investigate the fracture toughness of transition metal aluminium nitrides and their oxynitrides in pure bending (mode I) and shear (mode II). Furthermore, we study the effects of microstructure and crack path by using samples with columnar and fine-grained structures and then tilting the samples, such that the orientation of the internal interfaces relative to the loading direction is varied. In this way, we aim to reveal how far the fracture toughness can also be affected by forcing crack deflection in a single layer due to microstructural reasons rather than by employing a multilayer. We chose vanadium-based coatings for this investigation because in a previous study [54] these exhibited the highest Young's modulus among all tested materials. Moreover, it was possible to grow a (V, Al)(O, N) coating with a fine-grained

structure, whereas most transition metal nitride coatings normally exhibit a columnar structure. Sets of both coatings, (V, Al)N and (V, Al)(O, N), were deposited by HPPMS and DCMS with comparable chemical composition. As coatings from the HPPMS processing route showed normally a higher density [24], we use these two processing routes to study the effect of the density and strength of the column interfaces on the fracture toughness.

Experimental

Coating synthesis

(V, Al)N and (V, Al)(O, N) coatings were deposited in an industrial scale CemeCon CC 800/9 (Würselen, Germany) deposition system with utilisation of two Melec SIPP2000USB-10-500-S pulsers and 10 kW ADL GX 100/1000 DC power supplies. The chamber base pressure at the deposition temperature of $\sim 450^\circ\text{C}$ was below 0.7 mPa. V and Al targets ($>99.7\%$ purity) were assembled from two triangular pieces forming rectangular plates with dimensions $8.8 \times 50 \text{ cm}^2$. $10 \times 10 \text{ mm}^2$ Si(001) substrates were ultrasonically cleaned in acetone and ethanol prior to loading to the chamber and were mounted on a copper holder facing the targets at the target-to-substrate distance of 10 cm. The angles between the targets and substrate normal were $\sim 27^\circ$. Two different powering schemes were employed to deposit two series of (V, Al)N and (V, Al)(O, N) coatings.

In the first series, both targets were operated in DCMS mode (V/Al-DCMS). The gas flows during deposition were 160 sccm Ar and 80 sccm N_2 for (V, Al)N and 160 sccm Ar, 80 sccm N_2 , and 10 sccm O_2 for (V, Al)(O, N) resulting in partial pressures of 294, 147, and 2 mPa, respectively. The time-averaged powers of 2.4 kW for the V target and 2.5 kW for the Al target resulted in similar power densities of 6.9 to 7.1 W/cm^2 for both targets with and without presence of O_2 , respectively. A continuous direct current substrate bias potential of -70 V was employed throughout the deposition. The deposition time was kept at 90 min, resulting in the coating thickness of $\sim 3.0 \mu\text{m}$ for both nitride and oxynitride coatings.

In the second powering scheme, each target was operated by separate HPPMS power supplies, each using pulse on-time of $\tau_{\text{HPPMS}} = 50 \mu\text{s}$ at a duty cycle of 2.5%, corresponding to a pulsing frequency of $f = 500 \text{ Hz}$. Time-averaged powers of 2.4 kW for the V target and 2.5 kW for the Al target, similar to the DCMS mode, were used. The gas flows during deposition were 160 sccm Ar and 80 sccm N_2 for (V, Al)N and 160 sccm Ar, 80 sccm N_2 , and 5 sccm O_2 for (V, Al)(O, N), resulting in partial pressures of 294, 147, and 1 mPa, respectively. For (V, Al)N, peak power densities of 615 W/cm^2 for the V target and 510 W/cm^2 for the Al target were obtained, whereas 600 W/cm^2 for the V target and 520 W/cm^2 for the Al target were reached in the case

of (V, Al)(O, N). A pulsed substrate bias potential of -70 V was used to further densify the coatings through ion bombardment [26]. The pulse on-time of $\tau_s = 100$ μ s was synchronised with the HPPMS pulses at the targets with $+30$ μ s phase shift. The phase shift was considered to prevent acceleration of the gas ions generated at the beginning of the HPPMS pulses [22]. Coating thicknesses of ~ 2.7 μ m and ~ 2.5 μ m for (V, Al)N and (V, Al)(O, N), respectively, were obtained at a deposition time of 135 min.

The chemical composition was determined by energy dispersive X-ray spectroscopy (EDX) using a JEOL JSM-6480 scanning electron microscope (SEM) with an EDAX Genesis 2000 detection system at 12 kV acceleration voltage. One (V, Al)N [26] and one (V, Al)(O, N) coating analysed by time-of-flight elastic recoil detection served as standard for calibration of the EDX spectra. Structural analysis was done using a Bruker AXS D8 Discover General Area Detection Diffraction System (Billerica, MA, USA) with an incident angle of 15° . A Cu K α radiation source was used at a voltage and current of 40 kV and 40 mA, respectively. The coating microstructure was characterised using scanning transmission electron microscopy (STEM). Cross-sectional lamellae were prepared by focussed ion beam (FIB) techniques in an FEI Helios Nanolab 660 dual-beam microscope (Hillsboro, OR, USA). The same microscope was used for obtaining bright field (BF) micrographs with a STEM III detector at acceleration voltage and current of 30 kV and 50 pA, respectively. X-ray stress analysis was performed using the $\sin^2\psi$ method in a ψ geometry (ψ tilt axis in the diffraction plane), assuming a biaxial stress state [62]. Young's modulus E and nanoindentation hardness H were obtained in a Hysitron (Minneapolis, MN, USA) TI-900 TriboIndenter equipped with a Berkovich geometry-diamond tip with 100 nm radius. For each sample, a minimum of 50 quasistatic indents were performed, which resulted in contact depths of $<5\%$ with respect to the coating thickness. A fused silica standard was used to determine the tip area function and the load–displacement curves were analysed using the method of Oliver and Pharr [36].

Microcantilever fabrication

Microcantilevers were fabricated via FIB milling. First, a rough pre-cut of the cantilever shape with a beam current of 9.1 nA was made before the sample was turned by 90° for a back cutting. The back cutting was performed in three consecutive steps with beam currents of 9.1 nA, 0.79 nA, and 80 pA. After turning back to the surface, the notch was milled with the lowest ion current (80 pA). As last milling steps with 0.79 nA and 80 pA, the cantilevers were cut free and a shape refinement to the final dimensions was done. In general, the cantilever dimensions were chosen according to ASTM E399 [63] and following the suggestion from Matoy et al. [53] to keep the aspect ratios constant. The cantilevers had a cross section of approximately 1.8×1.8

μm^2 while the depth of the notch was 400–600 nm. Moreover, the distance of the notch to the cantilever base was approximately 2 μ m. The notch was maintained as a straight-through notch by first cutting the notch with some leftover material bridges but wider than the final cantilever width and then thinning the width of the cantilevers during the shape refinement until a straight-through notch resulted.

A more detailed description of the grain orientations used for the experiments can be found at the end of the manuscript in the methodology section. However, it is important to highlight that subsequent uses of the terms “parallel” and “perpendicular” are used with respect the growth direction of the coatings, and are not used in any crystallographic sense.

Microcantilever testing

The bending tests performed during this work and described in “Microcantilever bending” section were performed using an inSEM in situ nanoindenter (Nanomechanics, Inc., TN, USA) installed in a SEM type Clara (Tescan GmbH, Germany) and a diamond cube corner (provided by Synton MDP, Switzerland) with a constant displacement rate of 20 nm/s. For each datapoint reported, between four and six microcantilever bending tests were performed from which a mean value and standard deviation were calculated. For the evaluation of the load and displacement data, the Euler–Bernoulli beam theory [64] is used. From this, fracture stress σ at maximum load F can be calculated via:

$$\sigma = \frac{M}{I} = \frac{F(L\frac{W}{2})}{I} = \frac{F(L\frac{W}{2})}{(BW^3)/12} = \frac{6FL}{BW^2}, \quad (1)$$

$$I = \frac{BW^3}{12}, \quad (2)$$

where M is the bending moment at the load point, I the second moment of area, L the bending length (distance from load point to the notch), W the height, and B the width of the cantilever. An expression for the stress intensity factor K of a single edge cracked pure bending specimen is given by Murakami [65]:

$$K = \sigma^* \sqrt{\pi a f(a/W)}. \quad (3)$$

In this equation, a represents the notch depth and σ^* the characteristic stresses, e.g. for mode I the bending stress on the outer fibre and in mode II the shear stress on the crack plane. The term $f(a/W)$ is a dimensionless shape factor, which depends on the specimen dimensions and loading conditions. In this work we use the expression from Murakami [65] in the form:

$$f(a/W) = C_0 + C_1(a/W) + C_2(a/W)^2 + C_3(a/W)^3 + C_4(a/W)^4. \quad (4)$$

Bohnert et al. [47] used a finite elements model to fit the coefficients C_0 – C_4 to $C_0 = 1.05$, $C_1 = -1.14$, $C_2 = 5.60$, $C_3 = -9.33$, and $C_4 = 10.92$ for aspect ratios $0 < a/W \leq 0.6$. In this study,

the aspect ratio a/W is between 0.2 and 0.3 for all cantilevers, and we therefore use Eqs. (3) and (4) to calculate the fracture toughness for both modes. Defining the geometrical function $f(a/W)$ for mode I and mode II using the same bending stress as shown from Fett [66], we can express the difference between K_{Ic} and K_{IIc} only by the aspect ratio L/W . For a pure mode I geometry, the ratio L/W should be $L/W \geq 5$, while it should be $L/W \leq 1$ for mode II. The fracture toughness was calculated from the load–displacement curves from the experiment via Eq. (3), using the shape factor in Eq. (4). Furthermore, the data was corrected by several indents with varying maximum load but in the same range as maximum load during cantilever tests. This was done due to the sharp cube corner indenter which penetrates the surface of the cantilever. To correct the stiffness and displacement, the method suggested by Kupka and Lilleodden [67] was used.

Results

Composition, structure and mechanical properties

The measured chemical compositions of the DCMS and HPPMS grown (V, Al)N and (V, Al)(O, N) coatings are summarised in Table 1. These coatings are typically slightly over stoichiometric with respect to non-metals [16]. For (V, Al)N coatings, comparable chemical compositions were obtained under similar total partial pressures. Here, the sum of Ar and O impurities were below 1 at.%. The O_2 flow of 5 sccm in the HPPMS mode resulted in the O content of 13 at.% in the coating. However, due to lower ionisation degree in the DCMS mode, the O_2 flow needed to be increased to 10 sccm to obtain comparable O content of 11 at.% in the DCMS grown (V, Al)(O, N) coating. Phase formation of coatings deposited with both processing routes was probed by XRD and is shown in Fig. 1. The diffractograms show the formation of single-phase cubic structure (space group $Fm\bar{3}m$, NaCl prototype structure) without evidence for any secondary phase in the coatings. While the DCMS synthesised (V, Al)N coating shows a (111) texture, (V, Al)(O, N) as well as the coatings deposited by HPPMS exhibit a close to random orientation. In addition, the incorporation of O in the cubic structure of (V, Al)N seems to reduce the crystallinity of the quaternary compound.

The morphology of coatings is probed by cross-sectional BF-STEM and shown in Fig. 2. Both (V, Al)N coatings, deposited by DCMS and HPPMS processing routes, exhibit a columnar structure, as shown in Fig. 2. However, the coating grown by DCMS is characterised by pronounced columnar grain boundaries with partially underdense regions (bright regions along the columns) originating from limited surface diffusion during the growth. In a fully dense coating the number of grains per micron Fig. 2(e) multiplied with the average grain size Fig. 2(f) should result in one micron. However, for the DCMS deposited (V, Al)N this

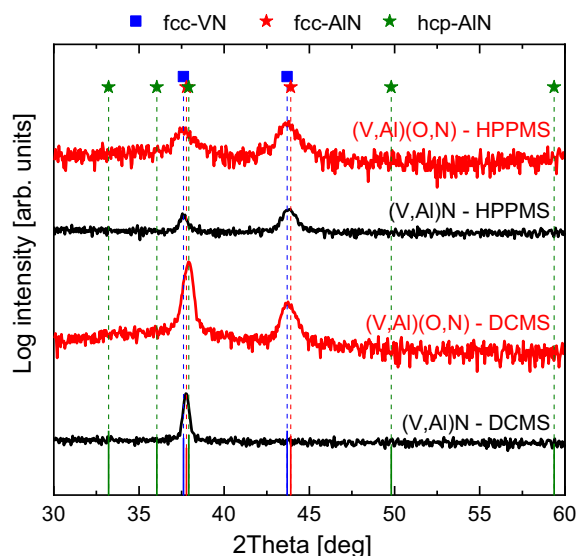


Figure 1: X-ray diffractograms of (V, Al)N and (V, Al)(O, N) coatings deposited by DCMS and HPPMS processing routes.

is only true for distances from the coating surface more than 900 nm. At lower distances from the coating surface a deviation up to 20% can be observed (near surface and decreasing with higher depth). Contrary, the higher peak power density in the HPPMS process increases the number of energetic particles arriving at the growing film surface, resulting in a higher adatom surface mobility and hence, a denser microstructure. For (V, Al)(O, N), the coating deposited by DCMS exhibits a columnar structure similar to the DCMS grown (V, Al)N coating. However, the population of the underdense regions is lower (less than 5%) than the comparable nitride coating. On the other hand, the (V, Al)(O, N) coating deposited by HPPMS process showed a distinct fine-grained structure with no evidence of underdense regions. Grain size and number of grains per micron and their standard deviations are calculated via line intersection method (10 lines per image).

Microcantilever bending

All measured fracture toughness values for different orientations and load cases are plotted against H^3/E^2 in Fig. 3. For better clarity and to avoid overlapping error bars in all sub-figures in Fig. 3, the data points are slightly shifted in positive or negative direction on the x -axis. Consequently, in Fig. 3(a) the coloured stripes that cover each data point of a coating are arrowed to show the coating's calculated H^3/E^2 -ratio, with the exact values given subsequently in Table 2. We find that the fracture toughness in mode II is consistently higher than in mode I for each material and orientation: with columns parallel to the loading direction, K_{IIc} is 20% to 30% higher and around 40% higher in the perpendicular orientation. For the

TABLE 1: Chemical composition of (V, Al)N and (V, Al)(O, N) coatings deposited by DCMS and HPPMS as characterised by standardised EDX.

Material system	Deposition route	V (± 1.1 at.%)	Al (± 1.3 at.%)	O (± 2.5 at.%)	N (± 2.5 at.%)
(V, Al)N	DCMS	24	26	–	50
(V, Al)(O, N)	DCMS	25	25	11	39
(V, Al)N	HPPMS	23	27	–	50
(V, Al)(O, N)	HPPMS	22	27	13	38

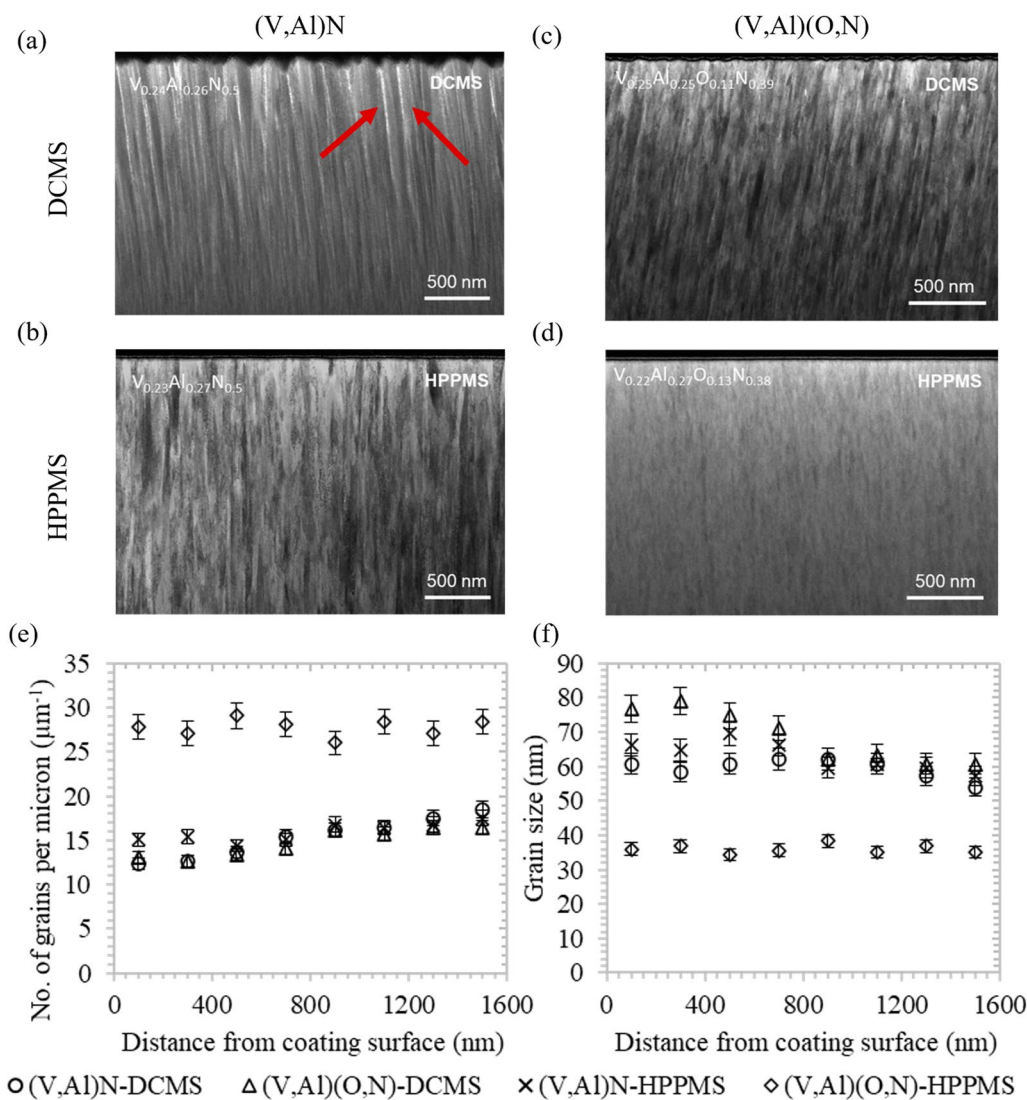


Figure 2: Cross section STEM micrographs for DCMS [(a) and (c)] and HPPMS [(b) and (d)]. In DCMS underdense regions can be found [white regions along columns exemplary highlighted with red arrows in (V, Al)N-DCMS]. (V, Al)(O, N)-HPPMS (d) exhibits fine-grained microstructure otherwise the growth was columnar. Additionally shown are the number of grains (e) and the grain size (f) plotted over the distance from the coating surface.

columnar structures, it was found that the fracture toughness decreases with an increasing H^3/E^2 -ratio. The trends between three materials are very similar regardless of the loading and orientation setup, with K_c decreasing by $\sim 25\%$ as H^3/E^2 increases by about 35%.

In the (V, Al)(O, N) sample with a fine-grained structure a higher K_{IIc} than K_{Ic} was also found (30% higher with parallel orientation and 35% higher in perpendicular orientation). However, when comparing the fracture toughness of the columnar structures, a difference between testing parallel and perpendicular to the growth direction was found: parallel to the growth direction

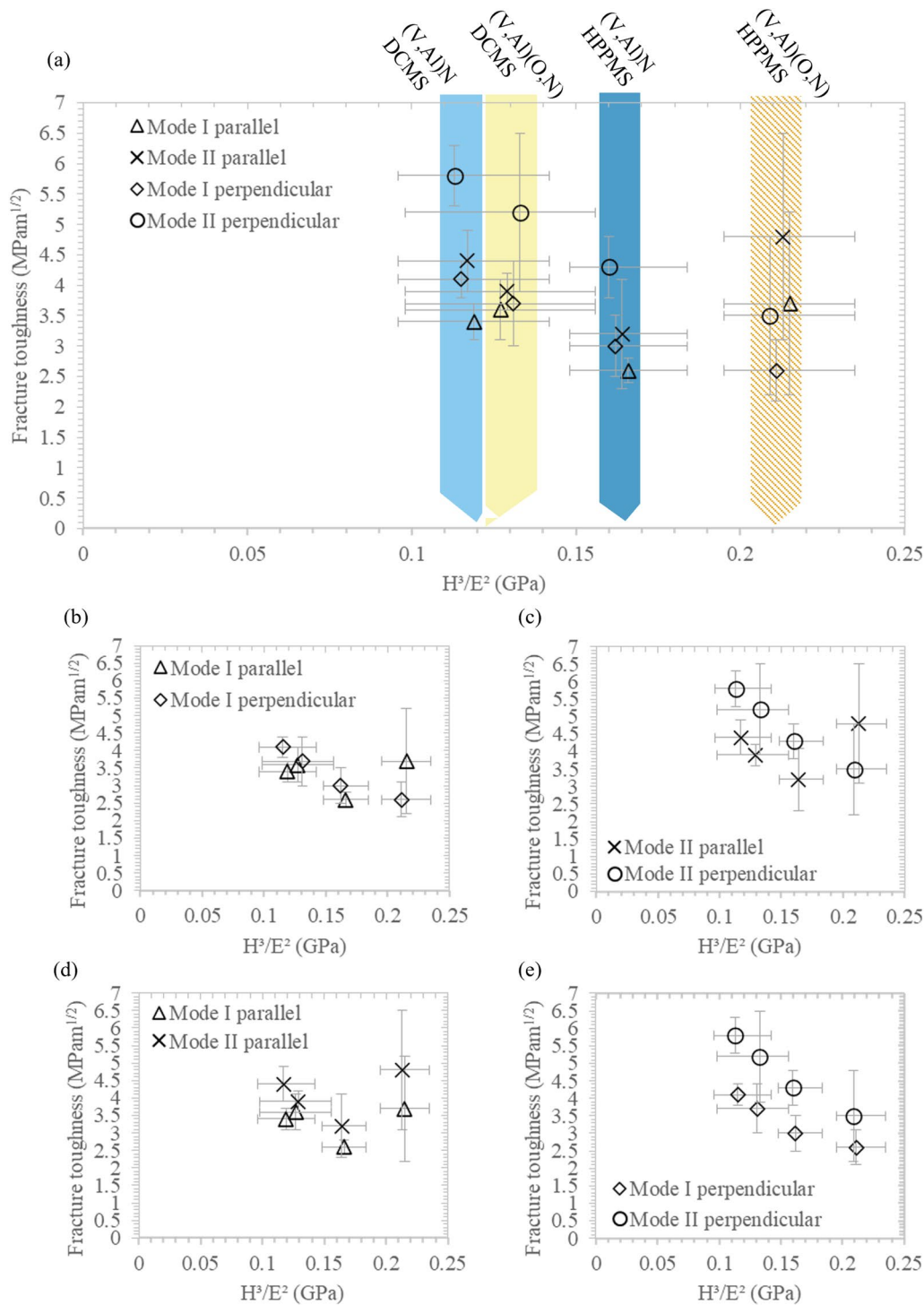


Figure 3: Fracture toughness over H^3/E^2 -ratio for all sample materials in mode I and mode II for two different orientations of the columns related to the growth direction (a). Subfigures pointing out parallel vs. perpendicular orientation [(b) and (c)] and mode I vs. shear [(d) and (e)].

the fracture toughness for the fine-grained sample is enhanced compared to the columnar structures, which showed a decreasing trend with a higher H^3/E^2 -ratio. This enhanced fracture toughness cannot be observed perpendicular to the growth direction where the fracture toughness of the fine-grained specimen

follows the same decreasing trend as in columnar structures. This leads to the result of a lower fracture toughness perpendicular to the growth direction than parallel to it in the fine-grained sample, while in all samples with columnar structure it is the opposite, and the parallel fracture toughness is lower.

TABLE 2: Overview of indentation hardness (H), indentation modulus (E), structure and measured fracture toughness for the four sample coatings in different directions.

Material	H^3/E^2 GPa	H GPa	E GPa	Coating thick- ness/beam width/notch depth $\mu\text{m}/\mu\text{m}/\text{nm}$	Parallel		Perpendicular		Structure
					K_{Ic} MPa ($\text{m}^{1/2}$)	K_{IIc} MPa ($\text{m}^{1/2}$)	K_{Ic} MPa ($\text{m}^{1/2}$)	K_{IIc} MPa ($\text{m}^{1/2}$)	
(V, Al)N DCMS	0.119 ± 0.023	25.8 ± 1.4	380 ± 20	$3.0 \mu\text{m}$ $2.0 \pm 0.1 \mu\text{m}$ $520 \pm 50 \text{ nm}$	3.4 ± 0.3 (5 Beams)	4.4 ± 0.5 (6 Beams)	4.1 ± 0.3 (6 Beams)	5.8 ± 0.5 (5 Beams)	Columnar
(V, Al)(O, N) DCMS	0.127 ± 0.029	25.5 ± 2.0	362 ± 6		3.6 ± 0.5 (6 Beams)	3.9 ± 0.3 (4 Beams)	3.7 ± 0.7 (5 Beams)	5.2 ± 1.3 (4 Beams)	Columnar
(V, Al)N HPPMS	0.166 ± 0.018	31.1 ± 0.9	426 ± 13	$2.7 \mu\text{m}$ $1.8 \pm 0.1 \mu\text{m}$ $480 \pm 50 \text{ nm}$	2.6 ± 0.2 (6 Beams)	3.2 ± 0.9 (5 Beams)	3.0 ± 0.5 (6 Beams)	4.3 ± 0.5 (5 Beams)	Columnar
(V, Al)(O, N) HPPMS	0.215 ± 0.021	32 ± 1.2	395 ± 9		3.7 ± 1.5 (4 Beams)	4.8 ± 1.7 (5 Beams)	2.6 ± 0.5 (4 Beams)	3.5 ± 1.3 (4 Beams)	Fine-grained

Comparing the crack path from scanning electron micrographs it can be seen that in mode I the crack is straight, running down along column boundaries or—in case of the fine-grained structure—along grain boundaries. Figure 4(a) and (b) show the crack path exemplary for (V, Al)N-DCMS, but for all others the same observation was made. However, in mode II the crack goes sideways and is cutting through the columns. Unfortunately, several attempts to lift out the remaining beams after fracture experiments were unsuccessful. Thus, straight imaging of the fracture surface was not possible and we will only discuss the side view. Furthermore, Fig. 4(c) to (f) show the fracture surfaces of all four coatings investigated in mode I. For both DCMS coatings, the columnar structure is visible, even though it has grown in an inclination in (V, Al)N. This inclination is also visible in Fig. 2(a) and (c). In both HPPMS coatings—for the columnar as well as the fine-grained oxynitride—the grain boundaries are densified and no longer distinguishable.

Discussion

In the course of this section we discuss our results in four parts. In the first part, we compare the differences in fracture toughness resulting from HPPMS and DCMS as a processing route. This comparison uses the mode I bending and mode II shear in the parallel orientation, only considering the columnar structures for the time being. Secondly, we focus on the differences from nitride to oxynitride and the effects of morphology on the fracture toughness and the crack path by comparing the fine grained (V, Al)(O, N) with the columnar (V, Al)N (both were deposited in HPPMS) and the columnar (V, Al)(O, N) deposited via DCMS. In the third part, we discuss the possibility to change the fracture behaviour by changing the morphology, concluding with part four comparing the parallel and perpendicular orientations.

All measured values we compare in this chapter are listed in the following Table 2 which corresponds to the data plotted in Fig. 3, hence, an identical colour code is used. These data are from beams in DCMS coatings (thickness $3.0 \mu\text{m}$) with a width of $2000 \pm 100 \text{ nm}$ and a notch depth of $520 \pm 50 \text{ nm}$. For HPPMS coatings (thickness $2.7 \mu\text{m}$) the beam widths were $1800 \pm 100 \text{ nm}$ and the notch depths were $480 \pm 50 \text{ nm}$. Beam widths and notch depths were measured individually on each beam before and after the bending experiment, respectively. The values given here are mean values with standard deviation (rounded).

Before starting with the analysis and discussion of the results obtained here, it should be pointed out again that the fracture behaviour of these coatings is mainly determined by the weakest bonding element. In this case, these are presumably the grain boundaries. Their bonding strength is dominated by grain boundary decoration and their bonding character. Both effects have already been investigated [68, 69]. In this paper, the effect of the microstructure on top of these effects will be investigated. For this purpose, grain boundaries with the same bond strength (each of the four coatings separately) but under different morphology (parallel or perpendicular to the growth direction) will be tested first. Subsequently, further effects such as the process route (HPPMS vs. DCMS), the chemical composition (nitride and oxynitride) or shear stress will be investigated in order to evaluate the effect in combination of these effects.

As will become apparent in the subsequent comparison of the different loading modes and orientations, the crack path during the fracture process has a significant influence on the final fracture toughness. For the expression of the stress intensity factor (Eq. 3) by Murakami [65] a homogeneous, brittle material is assumed. In this case—and as observed experimentally—the point of crack initiation from the pre-notch is also the point of critical failure, and there should be no need of further load to propagate the crack that grows straight through the material. As the geometrical factors remain unchanged, this therefore suggests that K_{Ic} is only a function of the initial notch length.

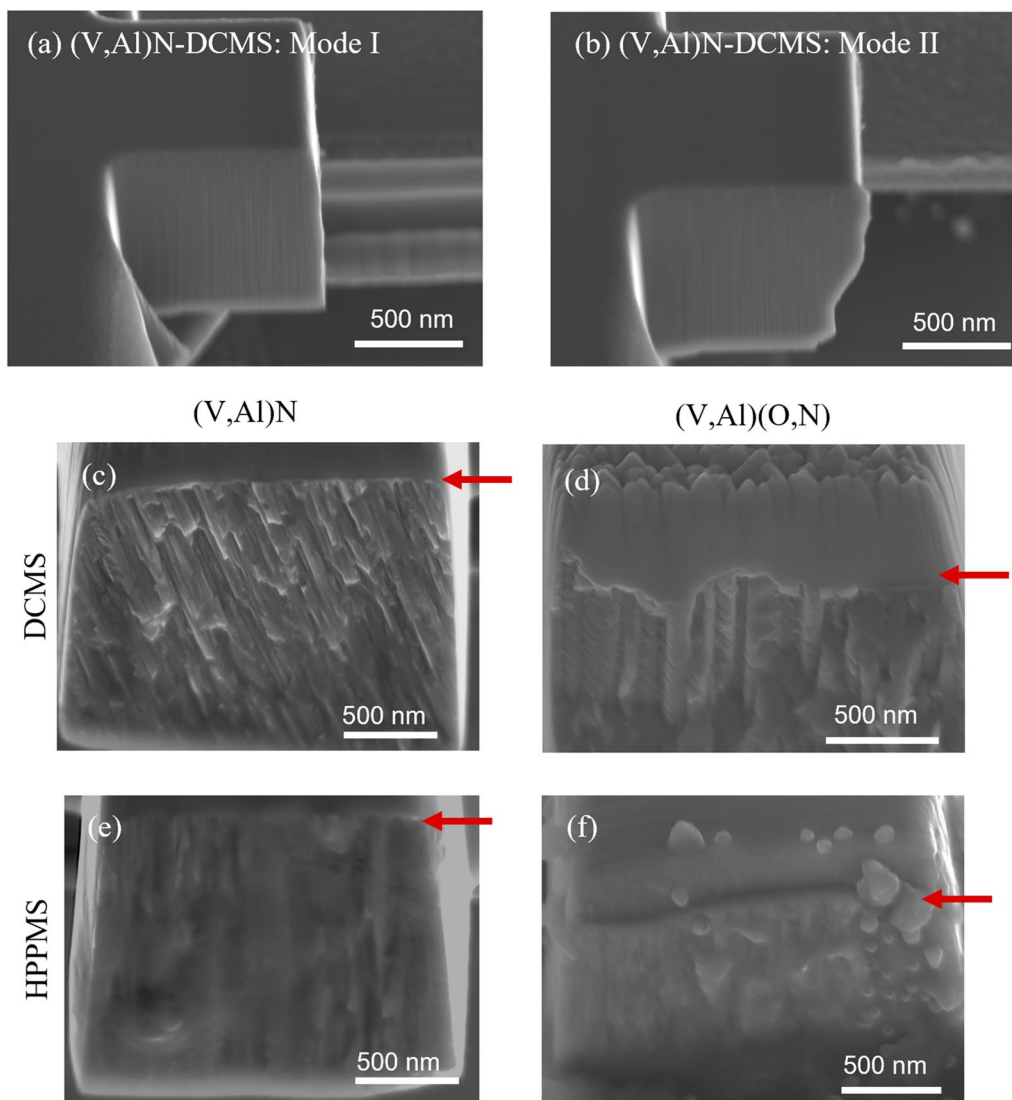


Figure 4: Crack path in (a) mode I and (b) mode II fracture exemplary shown in (V, Al)N-DCMS and (c) to (f) fracture faces (45° inclined) for all materials in mode I. Deepest position of notch (depth 400–600 nm) marked with red arrows; fracture face starts underneath. Note in the (V, Al)N materials in particular the field of view is such that the notch (and therefore the top of the beam) lies above the image.

However, these materials are not homogeneous. Crack deflection both reduces the stress intensity at the crack tip (i.e. K), as well as creating additional new surfaces with respect to a straight-through crack. While these effects are below the resolution of the intrinsically load-controlled machine—therefore no change in the shape of the stress–strain curve is observed—they do result in an increase in the final load and therefore the critical failure stress.

Comparing process routes

To compare HPPMS and DCMS we first concentrate on mode I and mode II tests in the parallel orientation. Here it is worth reiterating that samples from the DCMS deposition process exhibit

underdense regions that are more pronounced near the surface [Fig. 2(a)]. In contrast, the samples from the HPPMS process do not show such underdense regions [Fig. 2(b)]. Nevertheless, both types of samples show the same trend in fracture toughness between mode I and mode II, which can be explained by the fact that the porosity is mainly found in the uppermost approx. 500 nm. Since the notch depth is also around 400–600 nm, this region is almost removed in the active area of the specimen and thus no differences due to the near-surface underdense structure are observed.

Nevertheless, there are still a few deeper underdense regions in the DCMS structure, which could have significant effects on crack propagation. While the HPPMS process produces a denser coating with a corresponding 12% increase in indentation

modulus, the toughness of these coatings is around 25% lower. We speculate that this is due to the underdense regions in the tougher DCMS material causing a crack blunting effect when reached by a crack propagating from the upper surface, thus increasing the required load to cause failure.

A large difference is found between mode I and mode II fracture in the crack path. In mode I, the crack runs along the column boundaries [intergranular, Fig. 5(a)] while in mode II it intersects the columns [intragranular, Fig. 5(b)]. The plausibility of these observed crack paths is shown by the fact that the crack paths follow the direction of the highest resolved shear component, which is in mode I parallel to the load while in mode II the maximum is ideally under 45° to the load direction. For short beam shear tests on polymer matrix composites this was shown by Makeev et al. [70]. Here, due to the sharp indenter tip (cube corner) and the fact that it is not ideally positioned, the direction of the highest shear component deviates by a few degrees (less than 3°) from the ideal 45° . When the crack runs along the columns interfaces and is not cutting through the crystal, the measured fracture toughness values are representing the interface strength and will be dominated by grain boundary

decorations and bonding character. This is what we observe in the intergranular case of mode I. Consequently, the measured fracture toughness in the intragranular case (mode II) is more representative of the strength of the crystal itself.

In (V, Al)N the differences between mode I and mode II are found to be higher in DCMS. The fact that the difference between mode I and mode II is for (V, Al)N in HPPMS 6% less than in DCMS can be attributed to an increase in interface strength and density in HPPMS. Furthermore, the strength of the interface will be influenced by the residual stress of the coatings. In this study the HPPMS samples exhibit a compressive residual stress (-3.2 GPa for the nitride and -4.0 GPa for the oxynitride), while the DCMS coatings showed a slightly tensile one (0.7 GPa in the nitride and 0.5 GPa in the oxynitride). The measured indentation modulus and indentation hardness are clearly influenced by residual stresses, but the freestanding beams are typically considered to be stress free. However, their properties are nevertheless dependent on the stress as during the growth of the coating the interfaces can be influenced by residual stresses; during the coating process, compressive stresses can lead to compressed and thus denser grain boundaries. This can

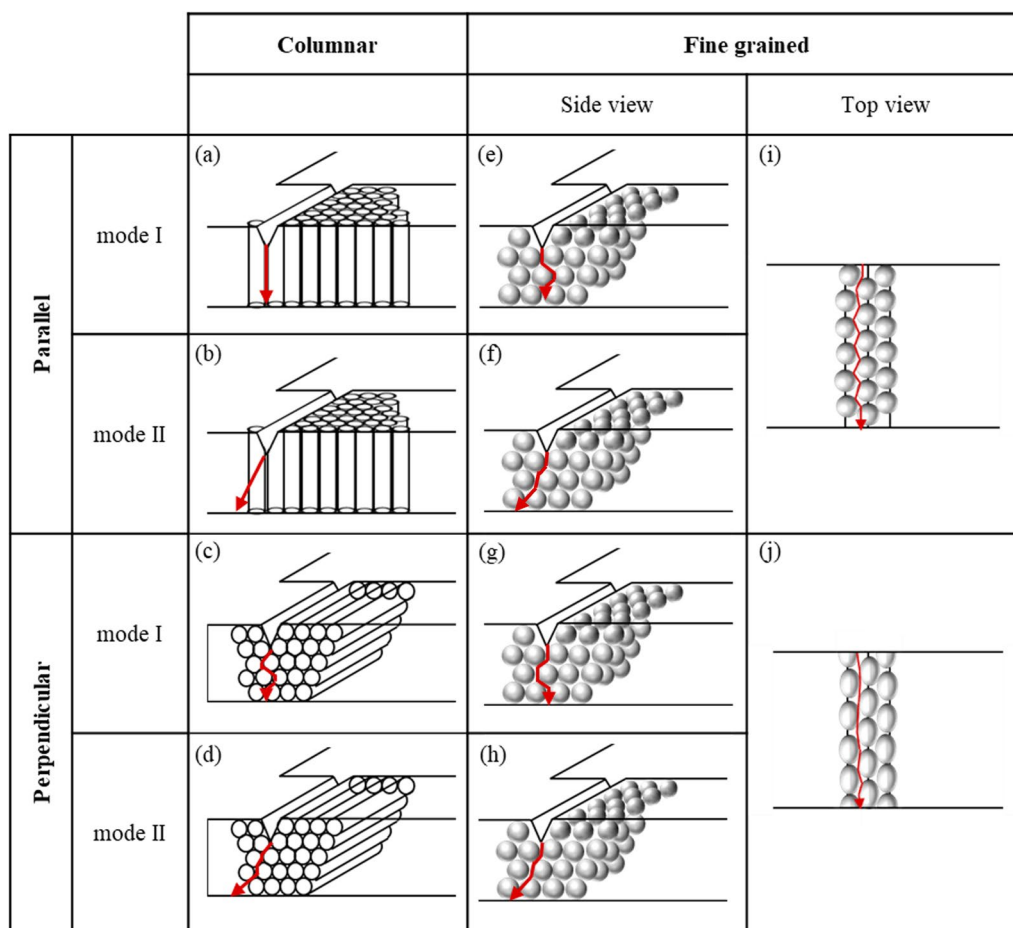


Figure 5: Schematic drawing of crack path for different fracture modes and orientations.

explain the small difference in fracture toughness between mode I and mode II measured here. The smallest difference between mode I and mode II was observed for (V, Al)(O, N) (DCMS) with a value of 8%. For the oxynitride various studies [16, 34, 57] showed that the introduction of oxygen leads to the formation of weaker M–O-bonds than M–N-bonds and compared to the pure nitride thus the Young's modulus decreases. This lowers the toughness of the material (mode II). Nevertheless, in all cases, the fracture toughness of the material is higher than that of the interfaces.

Trends in fracture toughness: nitride vs. oxynitride

For this section we compare first the nitride and oxynitride from the DCMS process and then the HPPMS ones using mode I fracture toughness for the parallel orientation. Nanoindentation revealed that the addition of oxygen resulted in a small, but measurable, reduction in Young's modulus for these materials. As mentioned above, DFT calculations show that this can be attributed to the formation of weaker M–O-bonds [16, 34, 57] compared with metal–nitrogen bonds. Correspondingly, two opposing predictions in the trends of fracture toughness can be hypothesised: on one hand, the Griffith criterion (Eq. 5) [71] shows for simple cleavage fracture that the fracture toughness is proportional to the Young's modulus and surface energy, thus predicting a lower fracture toughness for the oxynitride:

$$K_{Ic} = \sqrt{4 \cdot E \cdot \gamma}. \quad (5)$$

On the other hand, the H^3/E^2 -ratio for the oxynitrides would increase (as the hardness remains similar). With a higher H^3/E^2 -ratio at constant load the contact can more likely be considered as elastic. This was derived by Johnson's contact mechanics analysis, where it was shown that for flat surfaces in elastic/plastic contact the yield pressure linearly depends on H^3/E^2 [72, 73]. According to Chen et al. [74], the H^3/E^2 -ratio can be seen as an indication of resistance to plastic deformation, and may be a good indicator for fracture toughness, when there is no plasticity. Figure 3 clearly shows that this latter theory is an extremely poor predictor of fracture toughness, with K_{Ic} instead generally decreasing with an increasing H^3/E^2 -ratio. From a study on oxide glasses another interpretation of H^3/E^2 is derived. Smedskjaer and colleagues [75] suggested K_{Ic} to be seen as the resistance against (unstable) crack growth. From this we can assume underdense regions or fine-grained structures cause a barrier effect for the crack propagation, thus improving fracture toughness. In columnar structures without this effect, the crack can simply propagate along the column boundaries.

However, a simplistic application of the Griffith criterion (Eq. 5), is also a poor predictor of fracture toughness in this study. As it is known from nanolayers or nanocomposites, where the crack is frequently diverted along interfaces, there is a strong

effect of the microstructure that is not taken into account here, and is the reason why the fracture toughness does not strongly follow the trends in Young's modulus.

In the DCMS coatings, there are significant differences observed in the microstructure; where the nitride shows underdense regions, the oxynitride seems to be fully dense throughout the coating. Rather counterintuitively however, there is no significant difference in hardness and Young's modulus measured for both materials, nor any measured difference in fracture toughness (Table 2). There is the possibility that the oxygen might have formed an oxygen-rich grain boundary phase, densifying the coating and increasing the fracture toughness of the coating despite an intrinsically lower fracture toughness in the oxynitride itself. However, the TEM and EELS analyses to confirm this are beyond the scope of the present study. If we also consider the fracture toughness mode II from the previous "Comparing process routes" section, the conclusion could be that the incorporation of oxygen modifies the microstructure and grain boundaries. In this way, overall tougher (K_{Ic}) coatings are produced, although the intrinsic toughness (K_{IIc}) is proportionally lower.

The HPPMS coatings showed a different behaviour. Here the (V, Al)N exhibits a 12% higher Young's modulus, while having nearly the same hardness as the (V, Al)(O, N) (Table 2). Nevertheless, the oxynitride showed the higher fracture toughness, attributed to the fact that it was grown in a fine-grained structure and not the typical columnar structure.

Columnar structure vs. fine-grained

We now compare the fine-grained (V, Al)(O, N) from HPPMS with the DCMS oxynitride and the HPPMS nitride to differentiate between deposition methods and the resulting microstructure. This complex comparison is necessary as there is no columnar, HPPMS oxynitride to make a direct comparison between different microstructures.

In "Trends in fracture toughness: nitride vs. oxynitride" section we have already established that the relationship between fracture toughness and H^3/E^2 holds poorly and is strongly influenced by the microstructure. However, staying within the columnar structures, H^3/E^2 gives the resistance to crack propagation and the linear trend holds. Even if microstructural effects, such as underdense regions, result in a negative slope—contrary to the otherwise often observed positive trend, e.g. from Bartosik et al. [56]. Coatings deposited under similar conditions from a previous study [54] also fit into the negative trend observed here. Hence, assuming that the trend holds for the coatings used here, in case of a hypothetical columnar oxynitride manufactured with HPPMS we would expect a fracture toughness of around 1.2 MPa ($m^{1/2}$) by extrapolating a linear trend from the columnar grown coatings measured in this

study. The significant increase to 3.7 MPa ($\text{m}^{1/2}$) measured here in the fine-grained material can be attributed to the increase in crack path length in this microstructure. In principle, the crack paths in fine-grained and columnar beams point in the same direction. But in the fine-grained material, cracks can run along the grain boundaries in both parallel mode I and mode II, potentially changing direction in order to circumvent a grain rather than intersect it [as shown Fig. 5(e) and (f)]. Similar to crack deflection in a multilayer, this lengthens the crack path considerably. Therefore, despite the detrimental effect of oxygen on the mechanical properties discussed in "Trends in fracture toughness: nitride vs. oxynitride" section, this increase in crack path length explains the overall observation of a higher fracture toughness than predicted or in comparison to the (V, Al)N sample also deposited by HPPMS.

The enhancement in fracture toughness of ~200% by moving from a columnar to a fine-grained microstructure is, to the authors' knowledge, one of the largest increases in fracture toughness obtained solely through microstructural engineering. As a comparison, Daniel et al. showed a 50% increase in fracture toughness by moving from a columnar to a chevron structure [61]. This suggests that (if possible to manufacture) an equiaxed microstructure is optimal for producing a tough, protective coating.

Changing fracture properties by loading parallel or perpendicular to the growth direction

To achieve the same enhancement in fracture toughness as observed in fine-grained structure for columnar structures, we change the direction of the column growth relative to the loading direction. Seen schematically [Fig. 5(c) and (d)], the columnar structure looks similar to the fine-grained one [see Fig. 5(g) and (h)]. Even if the orientation of the columns is altered, the direction of the highest stress concentration remains unchanged, and thus also the general direction of crack propagation. However, comparing the results of columnar to fine-grained structures, it is found that now also in the columnar structure the cracks in both modes run intergranularly and must divert around individual columns. This explains the higher fracture toughness compared to the parallel orientation. Similar effects were previously observed in TiN when the morphology was changed from a columnar single layer to a multilayer chevron structure [61].

A significant difference between the fine-grained and columnar samples is seen in this comparison. In all the columnar materials, the corresponding toughness (K_{Ic} or K_{IIc}) is higher under perpendicular loading. The opposite is seen in the fine-grained material. In a hypothetical sample with truly equiaxed grains, no difference between parallel and perpendicular orientations would be expected to be observed [see the schematic Fig. 5(f) and (h)]. However, the shape of the grains in

the fine-grained sample are still slightly extended in the growth direction [also seen in Fig. 2(c)], as well as being slightly smaller than the grains forming the columns in the other materials. This is schematically shown in Fig. 5(i) and (j) (top view). One can see that due to this circumstance, the crack length and curvature are higher in the case of the parallel orientation. This explains the different behaviour compared to the columnar samples: in the fine-grained structure the larger extension of the grains is in perpendicular orientation and parallel to the crack propagation and therefore there is less deflection. For the columnar structures it is the other way around.

Optimising in-service performance of hard coatings

From an application point of view, there is usually a combination of compressive stresses perpendicular to the surface and shear stresses along the surface. From this study, this would correspond to mode I in parallel orientation (normal stress resistance) combined with mode II in perpendicular orientation (shear resistance). Consequently, the coating should have the best possible combination of hardness, Young's modulus, K_{Ic} parallel and K_{IIc} perpendicular. For example, if we look at the two DCMS samples, both have the required high K_{Ic} parallel and K_{IIc} perpendicular but only low hardness and Young's modulus. The (V, Al)N from the HPPMS process, on the other hand, has very high hardness and Young's modulus but only low fracture toughness. To better quantify this, our proposal is to use indices that evaluate resistance to crack propagation, hardness, Young's modulus and fracture toughness. From our measurements, this might be:

$$A = H^3/E^2 \cdot K_{Ic,parallel}; B = H^3/E^2 \cdot K_{IIc,perpendicular};$$

$$C = H^3/E^2 \cdot K_{IIc,parallel},$$

where the first part A represents the resistance against normal stress, the second part B the resistance to shear and the last part C is related to an intrinsic materials toughness. Consequently, these indices would have a dimension of $(\text{MPa})^2 (\text{m}^{1/2})$. Depending on the application indices A and/or B should be preferably high to improve the coating performance in terms of normal stress resistance or shear resistance. Index C is used here to address the change in interface strength by comparing it to index A , means that an intrinsic materials toughness (index C) is compared to the resistance against normal stress (index A). Via these indices the effects of different microstructures or crack blunting effects are included indirectly due to their influence in increasing the apparent fracture toughness of the material.

Of the samples investigated here, the fine-grained (V, Al)(O, N) sample produced in the HPPMS process had the best combination of properties—not the highest but high hardness and Young's modulus and high fracture toughness in mode I parallel and mode II perpendicular. This is reflected in the fact that the

indices proposed by us with $778 \text{ (MPa)}^2 \text{ (m}^{1/2})$ and $735 \text{ (MPa)}^2 \text{ (m}^{1/2})$ respectively are the highest from all samples investigated in this study (see Table 3).

Previously in "Comparing process routes" section, the relationship of the direction of crack propagation and the fracture toughness was mentioned. For a mode I fracture along the column boundaries, we would also measure the toughness of this interface, now represented by index A. In mode II, on the other hand, we measure more a toughness of the material due to the intragranular crack, which is now represented here by index C. Except for the HPPMS oxynitride, where due to the fine-grained structure also in mode II the crack is along the interfaces, but the crack path is elongated [see Fig. 5(f)].

If we compare those indices A and C for the two DCMS samples, we notice that, as expected (see also "Trends in fracture toughness: nitride vs. oxynitride" section), the oxynitride has a lower toughness of the material than the nitride, but a higher one at the interfaces. We therefore conclude that the oxygen incorporation modifies the grain boundaries. Comparing only the two nitrides from DCMS and HPPMS, there is hardly any change in the toughness of the material (index C). Since it is the same material, this was not unexpected, and as assumed an increase at the interfaces (index A) is measured for HPPMS. In the comparison of index A of the two HPPMS coatings, additionally the effect of the microstructure is recognisable. The change from nitride to oxynitride leads to a higher interface strength and at the same time to a crack deflection due to the change from columnar to fine-grained microstructure. Both together lead to the index A almost doubling for the oxynitride produced by HPPMS.

In conclusion, these indices allow a quantitative comparison of material performance and a method of ranking coatings based upon a balance of their mechanical properties. Based upon the expected stress state during application, performance based upon resistance to normal stresses (index A) and/or shear stresses (index B) can be evaluated. For materials development, index C provides the researcher with a parameter dominated by the intrinsic performance of a material. This allows the investigation of, for example, the effects of chemistry in a way that is decoupled from other toughening mechanisms such as using an

equiaxed microstructure to promote toughening through crack deflection.

Conclusion

In the course of this study, the fracture toughness of (V, Al)N and (V, Al)(O, N) was determined for different loading modes and morphologies as fine-grained or columnar structures. This was done to assess microstructural influences on fracture, in addition to the expected effects of grain boundary decoration and local bonding. For this reason, first coatings with the same presumed bonding strength of grain boundaries, i.e. identical coatings but tested in different directions, were investigated and then combinations of effects were studied. It was shown that of the materials studied, a fine-grained structure has the best combination of high hardness, high Young's modulus and high—but not the highest—fracture toughness and it is suggested to use an index including resistance to crack propagation via H^3/E^2 and toughness via $K_{Ic, \text{parallel}}$ and $K_{Ic, \text{perpendicular}}$ to quantify this. Based upon a balance of mechanical properties those indices allow a quantitative comparison of coating materials, at least those investigated within this study. It is of course expected that these proposed indices could be improved upon and they naturally require further validation on other systems.

However, this study also shows that changes to the microstructure can improve fracture toughness for a given hardness and Young's modulus. For example, crack deflection can be achieved in a single layer by using finer grains or a different orientation of columnar structures, leading to a behaviour similar to multilayer systems. The extreme case of "lying" columns applied here probably remains theoretical, but an inclination of the columns, as was also observed in this study for both DCMS coatings, can cause the same effect in a weakened form. Thus, even for samples with a columnar structure, property improvements can be induced by changes in the orientation of the microstructure. These combinations allow application-specific coating design: for example, an underdense coating may have a higher fracture toughness than a fully dense coating, but lower hardness and Young's modulus. A fully dense coating, on the other hand, can produce crack deflection and crack path elongation through inclined growth of the columns and thus increase fracture toughness. Moreover, the difference between nitride and oxynitride showed that stronger interfaces can contradict previously observed trends between indentation modulus and fracture toughness and can lead to higher overall coating toughness even when more brittle, lower modulus oxynitride materials are deposited.

Furthermore, measured by the difference between mode I and mode II in (V, Al)N it could be shown that compared to the DCMS processing route, HPPMS would produce stronger

TABLE 3: Suggested indices for normal stress resistance A, shear resistance B, and intrinsic materials toughness C for in this study tested specimen.

		(V, Al) N DCMS	(V, Al) (O, N) DCMS	(V, Al) N HPPMS	(V, Al) (O, N) HPPMS
A	$(\text{MPa})^2 \text{ (m}^{1/2})$	400	458	434	778
B	$(\text{MPa})^2 \text{ (m}^{1/2})$	690	656	713	735
C	$(\text{MPa})^2 \text{ (m}^{1/2})$	523	493	530	1008

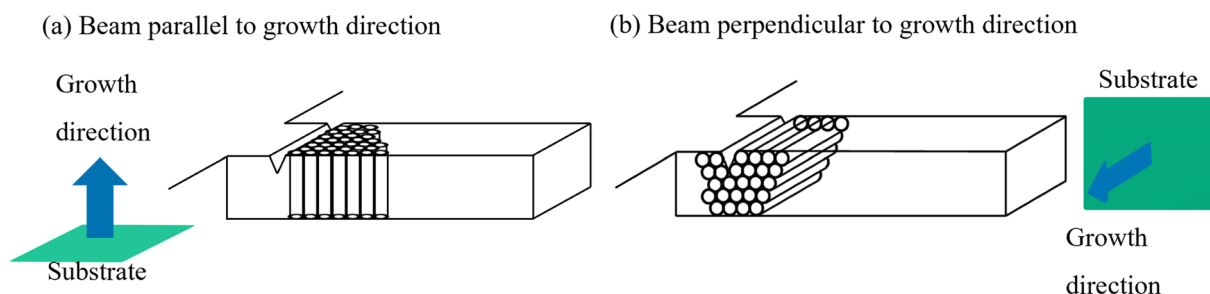


Figure 6: Schematic drawing of relation of column growth direction in the cantilever for samples with columnar structure.

interfaces by about 6% and thus might have an improved fracture toughness compared to a DCMS sample with the same hardness and Young's modulus, when no other effects such as microstructural defects influence the toughness. In this work, the DCMS deposited coatings showed the better fracture toughness due to a combination of microstructural effects in case of the nitride (underdense regions) and better interface strength in case of the oxynitride (lowest measured difference between mode I and mode II). Out of all coatings tested here the (V, Al)(O, N) deposited via HPPMS showed the best combination of fracture properties and mechanical properties as a result from stronger interfaces and fine-grained microstructure. Furthermore, all other tested specimens showed the potential of improved fracture properties by changing the morphology or strengthening the interface.

Finally, we have shown that these microstructural effects govern the experimentally determined mechanical behaviour. Predictions based on a simple linear crack path are inconsistent with the here reported experiments. In particular, the trends in fracture toughness run contrary to those predicted only by the H^3/E^2 -ratio of the materials. Thus we suggest to use indices combining fracture toughness and H^3/E^2 -ratio to rank the coatings performance in normal or shear stress.

Methodology

For each of the four coatings, one set of cantilevers was prepared from the surface and therefore parallel to the growth direction of the coating. For columnar structures, this means that all columns are parallel to the loading direction. A second set was prepared by turning the sample by 90°. In this way, the cantilevers are perpendicular to the growth direction and in case of columnar structures all columns are perpendicular to the loading direction. This is shown schematically in Fig. 6 and will be used to assess the differences in fracture behaviour depending on microstructure. In the following, we will refer to these orientations as parallel and perpendicular orientation which is independent from a crystallographic orientation.

Acknowledgments

The authors gratefully acknowledge the funding of the CRC TR 87 by the Deutsche Forschungsgemeinschaft (Project No. 138690629) within the part of "Mechanical Model" including Projects A3 and A6. Moreover, the authors acknowledge Professor Daniel Primetzhofer from Uppsala University for the time-of-flight elastic recoil detection measurement of the (V, Al)(O, N) sample used to calibrate the EDX.

Author contributions

Text, mechanical testing, imaging and data analysis: MRS. Coating deposition and determination of chemical composition, microstructure and mechanical properties (Parts 2.1 and 3.1): SKA. Supervision and review of experiments and manuscript: CFK, MH, JMS, SK-K and JSK-LG. Design of this study: SK-K and JSK-LG. Funding acquisition: SK-K and JMS.

Funding

Open Access funding enabled and organized by Projekt DEAL. This study was supported by the Deutsche Forschungsgemeinschaft (Project No. 138690629).

Data availability

The datasets generated during and analysed during the current study are available from the corresponding author on request.

Code availability

Not applicable.

Declarations

Conflict of interest Not applicable.

Open Access

This article is licensed under a Creative Commons Attribution 4.0 International License, which permits use, sharing, adaptation, distribution and reproduction in any medium or format,

as long as you give appropriate credit to the original author(s) and the source, provide a link to the Creative Commons licence, and indicate if changes were made. The images or other third party material in this article are included in the article's Creative Commons licence, unless indicated otherwise in a credit line to the material. If material is not included in the article's Creative Commons licence and your intended use is not permitted by statutory regulation or exceeds the permitted use, you will need to obtain permission directly from the copyright holder. To view a copy of this licence, visit <http://creativecommons.org/licenses/by/4.0/>.

References

1. E. Lugscheider et al., Investigation of the residual stresses and mechanical properties of (Cr, Al)N arc PVD coatings used for semi-solid metal (SSM) forming dies. *Thin Solid Films* **420–421**, 318–323 (2002)
2. K. Bobzin, N. Bagcivan, M. Ewering, Hartstoffsichten der Zukunft - Oxidische Schichten und HPPMS-Schichten für anspruchsvolle Zerspanaufgaben. *Dünne Schichten* **22**(6), 31–35 (2010)
3. K. Bobzin et al., Nitridische und oxinitridische HPPMS-Beschichtungen für den Einsatz in der Kunststoffverarbeitung (Teil 1). *Vak. Forsch. Praxis* **28**(6), 28–33 (2016)
4. K. Bobzin et al., Nitridische und oxinitridische HPPMS-Beschichtungen für den Einsatz in der Kunststoffverarbeitung (Teil 2). *Vak. Forsch. Praxis* **29**(1), 24–28 (2017)
5. P.H. Mayrhofer et al., 4.14—Protective transition metal nitride coatings. *Compr. Mater. Process.* **4**, 355–388 (2014)
6. H. Rueß et al., Effect of chemical composition, defect structure, and stress state on the elastic properties of $(V_{1-x}Al_x)_{1-y}N_y$. *J. Phys. Condens. Matter* **32**, 025901 (2020)
7. P.H. Mayrhofer, D. Music, J.M. Schneider, Influence of the Al distribution on the structure, elastic properties, and phase stability of supersaturated $Ti_{1-x}Al_xN$. *J. Appl. Phys.* **100**(9), 094906 (2006)
8. P.H. Mayrhofer, H. Willmann, A.E. Reiter, Structure and phase evolution of Cr–Al–N coatings during annealing. *Surf. Coat. Technol.* **202**, 4935–4938 (2008)
9. A. Hörling et al., Mechanical properties and machining performance of $Ti_{1-x}Al_xN$ -coated cutting tools. *Surf. Coat. Technol.* **191**, 384–392 (2005)
10. M. Baben et al., Unprecedented thermal stability of inherently metastable titanium aluminum nitride by point defect engineering. *Mater. Res. Lett.* **5**(3), 158–169 (2017)
11. W.S. Williams, High-temperature thermal conductivity of transition metal carbides and nitrides. *J. Am. Ceram. Soc.* **49**(3), 156–159 (1966)
12. R. Rachbauer et al., Temperature driven evolution of thermal, electrical, and optical properties of Ti–Al–N coatings. *Acta Mater.* **60**(5), 2091–2096 (2012)
13. A.D. McLeod, J.S. Haggerty, D.R. Sadoway, Electrical resistivities of monocrystalline and polycrystalline TiB_2 . *J. Am. Ceram. Soc.* **67**(11), 705–708 (1984)
14. J. Sjölen et al., Structure and mechanical properties of arc evaporated Ti–Al–O–N thin films. *Surf. Coat. Technol.* **201**(14), 6392–6403 (2007)
15. A. Khatibi et al., Structural and mechanical properties of Cr–Al–O–N thin films grown by cathodic arc deposition. *Acta Mater.* **60**(19), 6494–6507 (2012)
16. K.P. Shaha et al., Nonmetal sublattice population induced defect structure in transition metal aluminum oxynitrides. *Appl. Phys. Lett.* **103**, 221905 (2013)
17. K. Tönshoff et al., Performance of oxygen-rich TiALON coatings in dry cutting applications. *Surf. Coat. Technol.* **108–109**, 535–542 (1998)
18. A.P. Eghasarian et al., Influence of high power densities on the composition of pulsed magnetron plasmas. *Vacuum* **65**(2), 147–154 (2002)
19. V. Kouznetsov et al., A novel pulsed magnetron sputter technique utilizing very high target power densities. *Surf. Coat. Technol.* **122**, 290–293 (1999)
20. I. Petrov et al., Mass and energy resolved detection of ions and neutral sputtered species incident at the substrate during reactive magnetron sputtering of Ti in mixed Ar + N_2 mixtures. *J. Vac. Sci. Technol. A* **12**(5), 2846–2854 (1994)
21. K. Macák et al., Ionized sputter deposition using an extremely high plasma density pulsed magnetron discharge. *J. Vac. Sci. Technol. A* **18**(1533), 1533–1537 (2000)
22. G. Greczynski et al., Unprecedented Al supersaturation in single phase rock salt structure AlN films by Al^+ subplantation. *J. Appl. Phys.* **121**, 171907 (2017)
23. I. Petrov et al., Microstructural evolution during film growth. *J. Vac. Sci. Technol. A* **21**(5), S117–S128 (2003)
24. M. Samuelsson et al., On the film density using high power impulse magnetron sputtering. *Surf. Coat. Technol.* **205**, 591–596 (2021)
25. H. Hajihoseini, J.T. Gudmundsson, Vanadium and vanadium nitride thin films grown by high power impulse magnetron sputtering. *J. Phys. D* **50**, 505302 (2017)
26. S. Karimi Aghda et al., Unravelling the ion-energy-dependent structure evolution and its implications for the elastic properties of (V, Al)N thin films. *Acta Mater.* **214**, 117003 (2021)
27. J.-E. Sundgren, Structure and properties of TiN coatings. *Thin Solid Films* **128**(1–2), 21–44 (1985)
28. F. Giuliani et al., Deformation behaviour of TiN and Ti–Al–N coatings at 295 to 573 K. *Thin Solid Films* **688**, 137363 (2019)

29. A.E. Reiter et al., Investigation of the properties of $\text{Al}_{1-x}\text{Cr}_x\text{N}$ coatings prepared by cathodic arc evaporation. *Surf. Coat. Technol.* **200**, 2114–2122 (2005)
30. F. Jose et al., Significance of aluminum on hardness of titanium aluminum nitride deposited by magnetron co-sputtering. *Int. J. Ceram. Technol.* **6**(2), 243–248 (2009)
31. L. Zhou, D. Holec, P.H. Mayrhofer, First-principles study of elastic properties of cubic $\text{Cr}_{1-x}\text{Al}_x\text{N}$ alloys. *Appl. Phys. Lett.* **113**, 043511 (2013)
32. M. Bartosik et al., Fracture toughness and structural evolution in the TiAlN system upon annealing. *Sci. Rep.* **7**, 16476 (2017)
33. W.M. Seidl et al., Mechanical properties and oxidation resistance of $\text{Al-Cr-N/Ti-Al-Ta-N}$ multilayer coatings. *Surf. Coat. Technol.* **347**, 427–433 (2018)
34. S.J. Rotert et al., Theoretical study of elastic properties and phase stability of $\text{M}_{0.5}\text{Al}_{0.5}\text{N}_{1-x}\text{O}_x$ ($\text{M} = \text{Sc, Ti, V, Cr}$). *J. Appl. Phys.* **113**, 083512 (2013)
35. F. Rovere et al., Experimental and computational study on the phase stability of Al-containing cubic transition metal nitrides. *J. Phys. D* **43**, 035302 (2010)
36. W.C. Oliver, G.M. Pharr, An improved technique for determining hardness and elastic modulus using load and displacement sensing indentation experiments. *J. Mater. Res.* **7**(6), 1564–1583 (1992)
37. G.M. Pharr, W.C. Oliver, Measurement of thin film mechanical properties using nanoindentation. *MRS Bull.* **17**, 28–33 (1992)
38. S.J. Bull, Nanoindentation of coatings. *J. Appl. Phys.* **38**(R393), 393–413 (2005)
39. S.V. Hainsworth, H.W. Chandler, T.F. Page, Analysis of nanoindentation load–displacement loading curves. *J. Mater. Res. Lett.* **11**(8), 1987–1995 (1996)
40. J.J. Guo et al., Sample size induced brittle-to-ductile transition of single-crystal aluminum nitride. *Acta Mater.* **88**, 252–259 (2015)
41. S. Korte-Kerzel, Microcompression of brittle and anisotropic crystals: recent advances and current challenges in studying plasticity in hard materials. *MRS Commun.* **7**, 109–120 (2017)
42. M.F. Ashby, C.G. Sammis, The damage mechanics of brittle solids in compression. *PAGEOPH* **133**(3), 489–521 (1990)
43. J. Musil, M. Jirout, Toughness of hard nanostructured ceramic thin films. *Surf. Coat. Technol.* **201**, 5148–5152 (2007)
44. R. Soler et al., Fracture toughness of Mo_2BC thin films: intrinsic toughness versus system toughening. *Mater. Des.* **154**, 20–27 (2018)
45. S. Wurster, C. Motz, R. Pippan, Notched-cantilever testing on the micrometer scale—effects of constraints on plasticity and fracture behaviour. In: *18th European Conference on Fracture: Fracture of Materials and Structures from Micro to Macro Scale*, 2010
46. D. DiMaio, S.G. Roberts, Measuring fracture toughness of coatings using focused-ion-beam-machined microbeams. *J. Mater. Res.* **20**(2), 299–302 (2004)
47. C. Bohnert et al., Fracture toughness characterization of single-crystalline tungsten using notched micro-cantilever specimens. *Int. J. Plast.* **81**, 1–17 (2016)
48. F. Iqbal et al., In situ micro-cantilever tests to study fracture properties of NiAl single crystals. *Acta Mater.* **60**, 1193–1200 (2012)
49. A.K. Saxena et al., Experimental conditions affecting the measured fracture toughness at the microscale: notch geometry and crack extension measurement. *Mater. Des.* **191**, 108582 (2020)
50. J. Ast et al., Fracture toughness evaluation of NiAl single crystals by microcantilevers—a new continuous J-integral method. *J. Mater. Res.* **31**(23), 3786–3794 (2016)
51. M. Alfreider et al., In situ elastic–plastic fracture mechanics on the microscale by means of continuous dynamical testing. *Mater. Des.* **148**, 177–187 (2018)
52. K. Matoy et al., A comparative micro-cantilever study of the mechanical behavior of silicon based passivation films. *Thin Solid Films* **518**, 247–256 (2009)
53. K. Matoy et al., Interface fracture properties of thin films studied by using the micro-cantilever deflection technique. *Surf. Coat. Technol.* **204**, 878–881 (2009)
54. J.S.-K.L. Gibson et al., From quantum to continuum mechanics: studying the fracture toughness of transition metal nitrides and oxynitrides. *Mater. Res. Lett.* **6**(2), 142–151 (2018)
55. B. Völker et al., How tensile tests allow a screening of the fracture toughness of hard coatings. *Surf. Coat. Technol.* **390**, 125645 (2020)
56. M. Bartosik et al., Fracture toughness of Ti-Si-N thin films. *Int. J. Refract. Met. Hard Mater.* **72**, 78–82 (2018)
57. M. Hans et al., Effect of oxygen incorporation on the structure and elasticity of Ti-Al-O-N coatings synthesized by cathodic arc and high power pulsed magnetron sputtering. *J. Appl. Phys.* **116**, 093515 (2014)
58. E. Arzt, Size effects in materials due to microstructural and dimensional constraints: a comparative review. *Acta Mater.* **46**(16), 5611–5626 (1998)
59. Mitterer, C., PVD and CVD hard coatings. In: *Comprehensive Hard Materials* (Elsevier Ltd., Amsterdam, 2014), pp. 449–467
60. U. Helmersson et al., Growth of single crystal TiN/VN strained layer superlattices with extremely high mechanical hardness. *J. Appl. Phys.* **62**, 481 (1987)
61. R. Daniel et al., Grain boundary design of thin films: using tilted brittle interfaces for multiple crack deflection toughening. *Acta Mater.* **122**, 130–137 (2017)
62. M. Birkholz, P.F. Fewster, C. Genzel, *Thin Film Analysis by X-Ray Scattering*. *Front Matter* (Wiley-VCH, Weinheim, 2005)
63. ASTM, *Standard Test Method for Linear-Elastic Plane-Strain Fracture Toughness K_{Ic} of Metallic Materials*, ASTM E399-12 (ASTM, West Conshohocken, 2012), pp.1–33
64. C.M. Wang, Timoshenko beam-bending solutions in terms of Euler-Bernoulli solutions. *J. Eng. Mech.* **121**(6), 763–765 (1995)

65. Y. Murakami, *Stress Intensity Factors* (Pergamon Press, Oxford, 1987)
66. T. Fett, *Stress Intensity Factors and Weight Functions for Special Crack Problems*, FZKA 6025 (Technik und Umwelt, Karlsruhe, 1998), pp.1–40
67. D. Kupka, E.T. Lilleodden, Mechanical testing of solid–solid interfaces at the microscale. *Exp. Mech.* **52**, 649–658 (2011)
68. T. Glechner et al., Correlation between fracture characteristics and valence electron concentration of sputtered Hf–C–N based thin films. *Surf. Coat. Technol.* **399**, 126212 (2020)
69. C. Fuger et al., Revisiting the origins of super-hardness in TiB_{2+z} thin films—impact of growth conditions and anisotropy. *Surf. Coat. Technol.* **446**, 128806 (2022)
70. A. Makeev, Y. He, H. Schreier, Short-beam shear method for assessment of stress–strain curves for fibre-reinforced polymer matrix composite materials. *Strain* **49**, 440–450 (2013)
71. D. Gross, T. Seelig, *Bruchmechanik*, 6th edn. (Springer, Berlin, 2016)
72. B.D. Beake, The influence of the H/E ratio on wear resistance of coating systems—insights from small-scale testing. *Surf. Coat. Technol.* **442**, 128272 (2022)
73. K.L. Johnson, *Contact Mechanics* (Cambridge University Press, London, 1985)
74. X. Chen, Y. Du, Y.-W. Chung, Commentary on using H/E and H^3/E^2 as proxies for fracture toughness of hard coatings. *Thin Solid Films* **688**, 137265 (2019)
75. T. To, L.R. Jensen, M.M. Smedskjaer, On the relation between fracture toughness and crack resistance in oxide glasses. *J. Non-Cryst. Solids* **534**, 119946 (2020)

Publisher's Note Springer Nature remains neutral with regard to jurisdictional claims in published maps and institutional affiliations.